


Charge density waves and Fermi level pinning in monolayer and bilayer SnSe₂Shu-Ze Wang¹, Yi-Min Zhang¹, Jia-Qi Fan¹, Ming-Qiang Ren¹, Can-Li Song^{1,2,*}, Xu-Cun Ma^{1,2,†} and Qi-Kun Xue^{1,2,3,‡}¹State Key Laboratory of Low-Dimensional Quantum Physics, Department of Physics, Tsinghua University, Beijing 100084, China²Frontier Science Center for Quantum Information, Beijing 100084, China³Beijing Academy of Quantum Information Sciences, Beijing 100193, China (Received 10 September 2020; revised 8 December 2020; accepted 9 December 2020; published 22 December 2020)

Materials with reduced dimensionality often exhibit exceptional properties that are different from their bulk counterparts. Here, we report the emergence of a commensurate 2×2 charge density wave (CDW) in monolayer and bilayer SnSe₂ films by scanning tunneling microscopy. The visualized spatial modulation of the CDW phase becomes prominent near the Fermi level, which is pinned inside the semiconductor band gap of SnSe₂. We show that both CDW and Fermi level pinning are intimately correlated with band bending and virtual induced gap states at the semiconductor heterointerface. Through interface engineering, the electron-density-dependent phase diagram is established in SnSe₂. Fermi surface nesting between symmetry inequivalent electron pockets is revealed to drive the CDW formation and to provide an alternative CDW mechanism that might work in other compounds.

DOI: [10.1103/PhysRevB.102.241408](https://doi.org/10.1103/PhysRevB.102.241408)

A charge density wave (CDW) represents a static modulation of conduction electrons that is commonly accompanied by a periodic lattice distortion [1]. The understanding of such a collectively ordered electronic state has been widely supposed to be a key to decipher the secrets of unconventional superconductivity in many two-dimensional (2D) layered materials due to their close proximity in the electronic phase diagram [2,3]. In quest of this objective, dimensionality and interface engineering have been often considered as unique strategies to create and control the CDW phase [4–7]. As a matter of fact, newly emerging or enhanced CDW correlations have been revealed in several transition metal dichalcogenides at the 2D limit [8–11], whereas the interfacial effects on the CDW order of these 2D nanosheets were relatively little investigated [12,13]. A variety of scenarios invoking the saddle-point singularities [14], Fermi surface nesting [1,11], electron-phonon coupling [9], excitonic insulators [15,16], and Jahn-Teller band instabilities [10,17], as well as some combination of them [18], have been employed to account for the formation of CDW. However, a consensus on which factors play the primary roles in driving the CDW transition remains a hotly debated topic.

On the other hand, layered main-group metal dichalcogenides such as SnSe₂ have recently attracted substantial interest owing to their potential applications in field-effect transistors [19], and optoelectronic [20,21] and thermoelectric devices [22], while the high abundance and low toxicity of Sn hold promises for commercial use. Interface engineering via organometallic intercalation [23,24], heterostructure design [25,26], and dielectric gating techniques [27] has led to the emergence of superconductivity in SnSe₂, although its bulk counterpart is well known as a semiconductor with an

indirect band gap of 1.07 eV [28]. Moreover, periodic lattice distortions, possibly associated with CDW, were reported in pressurized and compressed SnSe₂ [26,29]. Astonishingly, the so-called CDW orders exhibit different wave vectors, calling for further study. Layered 1T-SnSe₂ has thus become a newly fertile playground for the exploration and manipulation of these many-body collective phenomena, as well as the interplay between them. In this Rapid Communication, we employ scanning tunneling microscopy (STM) to exploit interface-induced CDW order and Fermi level (E_F) pinning in monolayer (ML) and bilayer (BL) SnSe₂ films prepared on Sn-terminated Si(111) and SrTiO₃(001) substrates. Virtual induced gap states (VIGSs) at the semiconductor heterointerface are visualized and found to correlate intimately with the occurrence of CDW and E_F pinning in ultrathin SnSe₂.

All experiments were carried out in an ultrahigh vacuum cryogenic STM system (Unisoku), which is connected to a molecular beam epitaxy (MBE) system for *in situ* sample preparation. The base pressure of both chambers is better than 1.0×10^{-10} Torr. Arsenic-doped Si(111) wafers were cleaned by repeated flashing to 1200 °C, leading to a reconstructed Si(111)- 7×7 surface, while niobium-doped SrTiO₃(001) substrates were heated at 1200 °C for 20 min to get a clean surface. High-purity Sn (99.9999%) and Se (99.999%) sources are coevaporated from standard effusion cells onto the substrates at 210 °C [25]. Due to the very volatile nature of Se molecules from the effusion cell, a high Se/Sn flux ratio of ~ 10 was used to compensate for the Se losses during the MBE growth, bearing a similar growth dynamic to that for other metal selenides [30]. After the film growth, the samples were immediately transferred into the STM stage for data collection at 4.5 K, unless otherwise specified. Polycrystalline PtIr tips were conditioned by electron beam heating, calibrated on Ag/Si(111) films, and used throughout the experiment. Tunneling conductance spectra were measured by using a standard lock-in technique with a small bias modulation at 931 Hz.

*clsong07@mail.tsinghua.edu.cn

†xucunma@mail.tsinghua.edu.cn

‡qkxue@mail.tsinghua.edu.cn

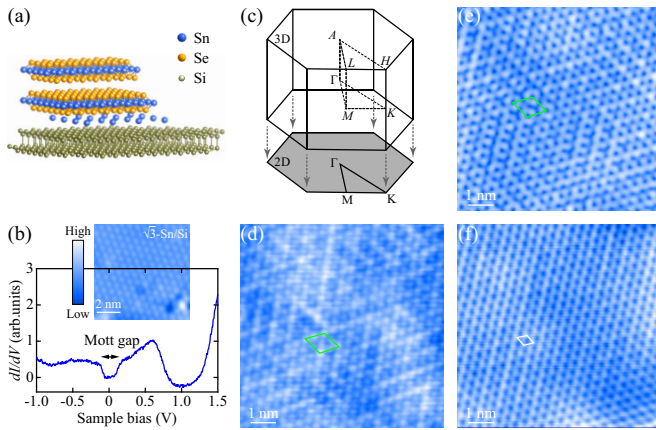


FIG. 1. (a) Sketch of $1T$ - SnSe_2 (space group: $P\bar{3}m1$) films on Sn-terminated Si(111). (b) Differential conductance dI/dV spectrum showing a Mott-Hubbard gap of ~ 0.26 eV around E_F in $\sqrt{3}$ -Sn/Si. The set point is stabilized at $V = 1.6$ V and $I = 100$ pA. Inserted is a representative STM image of the $\sqrt{3}$ -Sn/Si surface (8 nm \times 8 nm, $V = -1.8$ V, $I = 100$ pA). (c) 3D and 2D Brillouin zones of SnSe_2 . (d)–(f) STM topographies of ML, BL, and TL SnSe_2 films epitaxially grown on $\sqrt{3}$ -Sn/Si (8 nm \times 8 nm), respectively. The white and green rhombuses mark the primitive and charge order unit cells, respectively. Imaging conditions are $V = 0.5$ V and $I = 100$ pA, except for (e) $V = 0.2$ V.

Layered $1T$ - SnSe_2 has a trigonal symmetry and consists of hexagonally packed Sn sheets sandwiched between the anionic Se sheets with an in-plane lattice parameter of approximately 3.81 Å [28]. In order to optimize the epitaxial growth of SnSe_2 thin films, freshly cut Si(111) substrates with an in-plane lattice parameter of 3.8403 Å are ideally chosen [Fig. 1(a)], yielding a lattice mismatch of $< 0.8\%$. We further passivate the chemically reactive Si(111)- 7×7 substrates by depositing $\sim 1/3$ ML Sn atoms at 600°C , as detailed in the Supplemental Material [31]. This results in a Sn-terminated Sn/Si(111)- $\sqrt{3} \times \sqrt{3}R30^\circ$ (hereafter referred

to as $\sqrt{3}$ -Sn/Si) surface, characteristic of a Mott-Hubbard insulating ground state [Figs. 1(b) and S1] [32,33]. Figure 1(c) depicts the three-dimensional (3D) Brillouin zone of SnSe_2 with high symmetry points and its 2D projection. Recent first-principles calculations and band-structure measurements of SnSe_2 have located its conduction band minimum (CBM) and valence band maximum (VBM) along the M - L and Γ - M (K) directions [28,34], respectively. This differs from the CDW-bearing sister compound $1T$ - TiSe_2 with the VBM located just at Γ [13]. In addition, TiSe_2 has been widely considered to be a semimetal or a narrow-gap semiconductor [15,18,34], whereas the semiconducting SnSe_2 exhibits a gap greater than 1.0 eV [28]. Despite these distinctions, ML and BL SnSe_2 films grown on $\sqrt{3}$ -Sn/Si exhibit a clear charge order [Figs. 1(d) and 1(e)]. In analogy to $1T$ - TiSe_2 , the CDW modulation displays a commensurate 2×2 structure. More remarkably, the CDW vanishes in triple-layer (TL) SnSe_2 , leaving behind an intact $\text{SnSe}_2(001)$ - 1×1 surface [Fig. 1(f)].

Provided that the lattice mismatch between SnSe_2 and the Si(111) substrate is negligibly small, we exclude that the observed CDW phase originates from any possible effects associated with the epitaxial strain [26]. To understand the microscopic cause of the CDW order, we show a series of bias-dependent STM topographies and the corresponding fast Fourier transform (FFT) images in Figs. 2 and S2. Evidently, the CDW spots, marked by the green circles, become more prominent near E_F . This is understandable since a CDW phase transition mainly affects the density of states (DOS) of SnSe_2 close to E_F . More interestingly, the CDW wave vector q_{CDW} reduces below -0.1 eV (Fig. S3), leading to a crossover from a commensurate to incommensurate CDW state.

Figure 3(a) plots the CDW intensity (top panel), calculated as the integrated FFT magnitude from the green circled regions in Fig. 2(b), as a function of the bias. As expected, the CDW is suppressed at an elevated temperature of 78 K. Compared to BL SnSe_2 , ML SnSe_2 displays more pronounced CDW. This hints at the essential importance of interfacial effects in the CDW formation. A careful investigation of

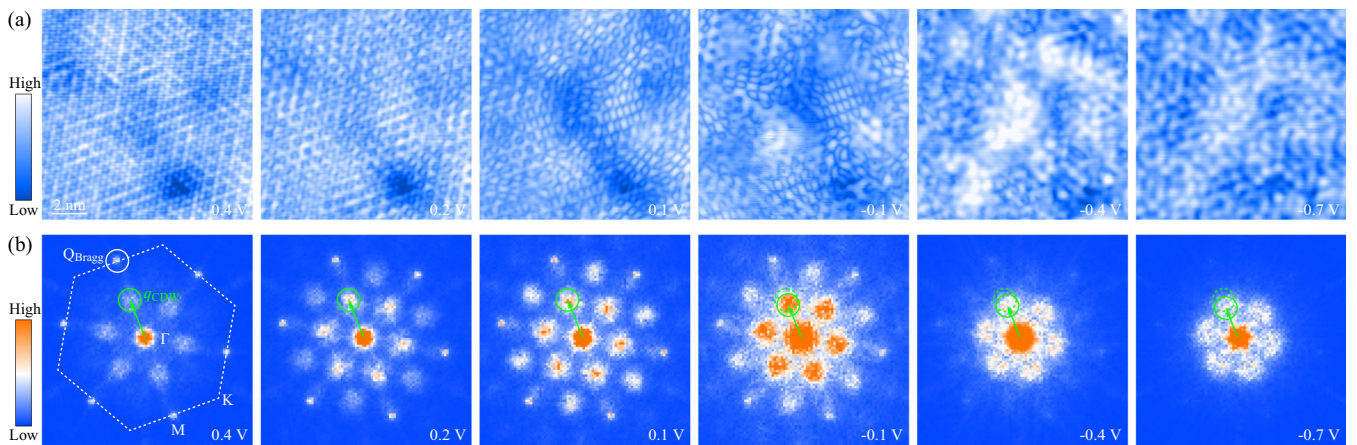


FIG. 2. (a) Constant-current STM topography images of monolayer $\text{SnSe}_2/\sqrt{3}$ -Sn/Si films in the same field of view (12 nm \times 12 nm, $I = 100$ pA) and (b) the corresponding FFT amplitudes at the indicated sample biases. Every FFT image has been sixfold symmetrized to optimize the signal-to-noise ratio. The Bragg peaks and CDW spots of SnSe_2 are white and green circled, respectively. The white hexagon in the left FFT image corresponds to the 2D Brillouin zone of SnSe_2 , while the three dashed circles denote the 2×2 CDW spots just as the FFT images on the left. Note that the green arrows mark the CDW wave vectors that gradually decrease below -0.1 eV.

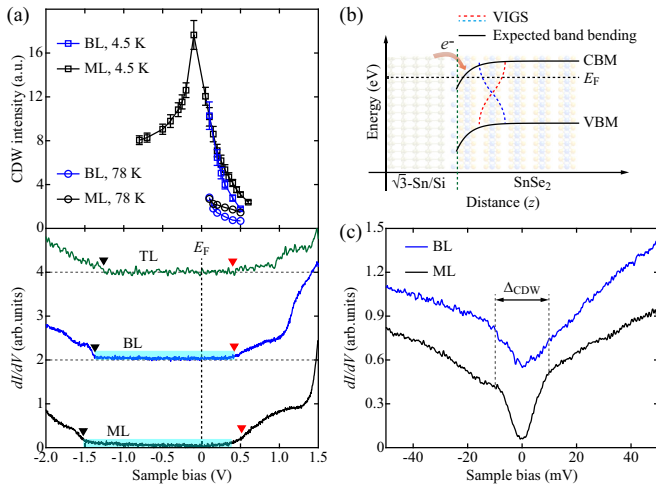


FIG. 3. (a) Energy-dependent CDW intensity (top panel) and wide-energy-scale dI/dV spectra ($V = 1.5$ V, $I = 100$ pA) at varied film thicknesses (bottom panel). The black (red) triangles mark the VBM (CBM) near Γ , with their spacing corresponding to the direct band gap $E_g^{\text{dir}}(\Gamma)$ of SnSe₂. The vertical dashed line denotes E_F throughout, and the cyan rectangle indicates emergent in-gap states. (b) Energy band diagram for the SnSe₂/ $\sqrt{3}$ -Sn/Si semiconductor heterointerface, as well as the interfacial origin of the in-gap states. (c) Tunneling spectra showing CDW energy gaps near E_F on both ML and BL SnSe₂.

SnSe₂ thickness-dependent dI/dV spectra in the bottom panel of Fig. 3(a) reveals an enhancement of the direct band gap $E_g^{\text{dir}}(\Gamma)$ upon reduction of the film thickness. This is consistent with a previous report [25] and could be accounted for in terms of the poor electrostatic screening and enhanced quantum confinement in few-layer SnSe₂ [28]. More significantly, we find that on the surface E_F is pinned ~ 0.4 – 0.5 eV below the CBM at Γ , irrespective of the SnSe₂ film thickness.

The formation of the CDW phase and E_F pinning in ultrathin SnSe₂ films are closely related to the emergent electronic states in the semiconducting gap, i.e., the cyan-marked finite DOS in Fig. 3(a). The in-gap states get suppressed with thickness and could not be ascribed to any impurity-induced bound states, because there exists little defect on the SnSe₂ films investigated [Figs. 1(d)–1(f)]. Knowing that SnSe₂ has a large electron affinity [35], upon contact electrons would flow from $\sqrt{3}$ -Sn/Si to SnSe₂, leading to downward band bending of the SnSe₂ and confinement of 2D electron gas (2DEG) at the interface [Fig. 3(b)]. This might contribute to some in-gap states predominantly near the CBM at the M points of the 2D Brillouin zone. More significantly, VIGSs will develop at the SnSe₂/ $\sqrt{3}$ -Sn/Si semiconductor heterointerface and extend over the whole indirect band gap of SnSe₂ [36]. The VIGSs correspond to the imaginary components of the complex wave function and exponentially decay away from the interface [36]. As predicted, the decay lengths critically rely on the energy and diverge at the conduction and valence band edges for the VIGSs with conduction band character and valence band character, respectively. As a consequence, more conduction (valence)-derived VIGSs emerge around CBM and VBM, marked by the red (blue) dashed lines in Fig. 3(b). Based on the one-dimensional VIGS model [37], the minimum decay

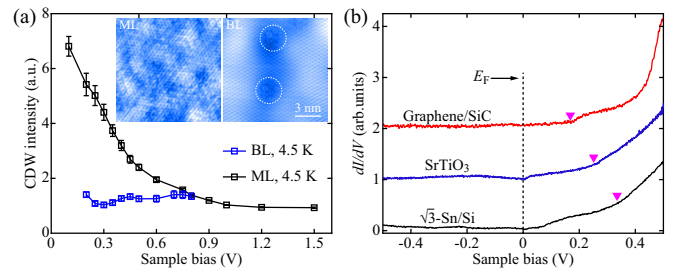


FIG. 4. (a) Calculated CDW intensity of ML and BL SnSe₂ films on the SrTiO₃ substrate. Insets are STM images (12 nm \times 12 nm, $V = 0.3$ V, $I = 100$ pA) of ML and BL SnSe₂ films on SrTiO₃, with the dashed circles embracing the short-range CDW in the vicinity of defects. (b) Comparison among dI/dV spectra ($V = 0.5$ V, $I = 100$ pA) of ML SnSe₂ films on different substrates, measured in an energy range of ± 0.5 eV. The magenta triangles represent the CBM at the M point of the 2D Brillouin zone in SnSe₂.

length of VIGSs occurs roughly at the midgap energy and approximates to 6.0 Å for SnSe₂. This is consistent with the sharply suppressed in-gap states on BL and TL SnSe₂ [see the bottom panel of Fig. 3(a)]. Plotted in Fig. 3(c) are the smaller-energy-scale tunneling spectra of ML and BL SnSe₂ films. Partial gaps associated with the CDW phase are identified in the vicinity of E_F . The gap magnitude $\Delta_{\text{CDW}} \sim 20$ meV agrees quantitatively with the significant suppression of CDW at 78 K [Fig. 3(a)].

In order to provide more insights into the CDW phase of SnSe₂, we also prepare ultrathin SnSe₂ films on a SrTiO₃ substrate. Distinct from a recent report [26], no apparent lattice compression is revealed. This seems more understandable because the MBE growth of layered SnSe₂ films is of quasi-van der Waals epitaxy. Shown in Fig. 4(a) are STM topographies and energy-dependent CDW intensities in ML and BL SnSe₂/SrTiO₃ films. Evidently, the CDW modulations are weaker than those in SnSe₂/ $\sqrt{3}$ -Sn/Si. In particular, only short-ranged CDW order, circled by the white dashes in Fig. 4(a), could be seen to surround single native defects in BL SnSe₂/SrTiO₃ films.

Figure 4(b) compares the tunneling dI/dV spectra of monolayer SnSe₂ films on the indicated substrates, with the MBE growth of SnSe₂ on the graphene/SiC substrate described in detail elsewhere [25]. The conductance kinks, marked by magenta triangles, correspond to the CBM at M . The emergence of VIGSs proves generic for all three heterostructures and serve as a reservoir for electrons/holes. These states effectively pin E_F and hold the key for the CDW formation in ML and BL SnSe₂. Given that the band bending and VIGS decay length are determined primarily by the semiconductor parameters of SnSe₂ [37,38], the smaller energy spacing between the CBM at the M points and E_F means more electron doping. Such a distinction may be probably related to the different work function of the substrates. Regardless, our comparison study enables us to establish a doping-dependent phase diagram of SnSe₂ in Fig. 5(a). Upon electron doping via interface engineering, the CDW develops with the filled VIGSs in the ML and BL SnSe₂/ $\sqrt{3}$ -Sn/Si films. As the electron doping is further increased, the CDW phase gets suppressed in ultrathin SnSe₂/SrTiO₃ films and eventually

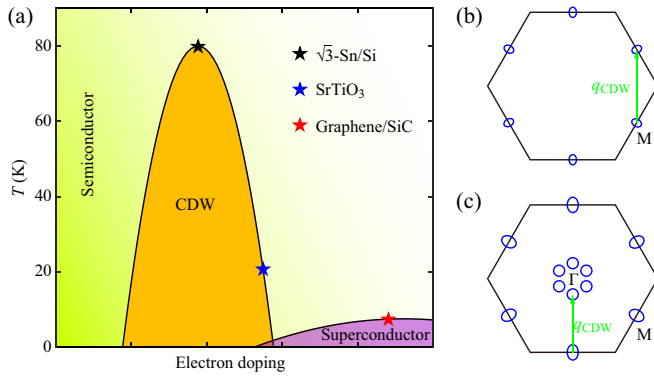


FIG. 5. (a) Electronic phase diagram of SnSe₂. The stars denote monolayer SnSe₂ films on $\sqrt{3}$ -Sn/Si, SrTiO₃, and graphene/SiC substrates, respectively. (b) Fermi surface and (c) constant energy contour (i.e., the midgap energy level) of SnSe₂ films. The black hexagons denote the 2D Brillouin zone of SnSe₂, while green arrows the q_{CDW} of CDW order.

evolves into a superconducting state when the SnSe₂ films are grown on a graphitized SiC(0001) substrate [25]. This complete electronic phase diagram highlights the importance of dimensionality and electron doping in SnSe₂ semiconductors, and offers fresh insights into the relationship between the CDW phase and superconductivity.

We now discuss the possible mechanisms for the observed CDW phase. The large semiconductor band gap of 1.07 eV prevents an excitonic insulator scenario from being responsible for the CDW order in SnSe₂, where an exciton binding energy larger than the band gap is needed but hardly fulfilled [15]. This holds even more true for ultrathin SnSe₂ films with an enhanced band gap [Fig. 3(a)]. Second, a Jahn-Teller band instability, as widely explored for explaining CDW in Ti-based dichalcogenides [10,39,40], could be safely excluded as well. This is primarily because a starting point of the band-type Jahn-Teller interaction is the substantial overlap of conduction and valence bands, which is yet separated by the semiconductor band gap in SnSe₂. Moreover, this model relates intimately to a low-lying *d*-orbital splitting [41] or an *s-d* orbital mixing [17]. Distinct from TiSe₂, however, the *d* orbital is little involved in the conduction and valence bands of the *s-p* metal dichalcogenide SnSe₂ [28]. As thus, our results call for other scenarios for the formation of CDW in SnSe₂. Obviously, any models associated with saddle-point singularities are unlikely, since E_F of the SnSe₂ films is well pinned inside the band gap and no sharp DOS enhancement is observable around E_F [Figs. 3(a) and 4(b)].

Next, we resort to a classical concept of CDW order induced by Fermi surface nesting [1]. This is in agreement with our observation of CDW only in the presence of sufficient in-gap states or electronic DOS around E_F . Multilayered and bulk SnSe₂ without low-lying DOS exhibits no CDW.

Since E_F of ultrathin SnSe₂ films lies closer to the CBM(M) than VBM(Γ), the electronic DOS in the vicinity of E_F originates predominantly from the band bending confined two-dimensional electron system (2DES) and VIGSs with conduction-band character at M , illustrated in Fig. 5(b). There exists little DOS at Γ , and thus a simple Fermi surface nesting connecting the CBM(M) than VBM(Γ) seems unlikely. Alternatively, the Fermi surface nesting between symmetry-inequivalent electron pockets at M , marked by the green arrow in Fig. 5(b), might be the driving force for the CDW formation. This is especially true as the electron pockets are small and the Fermi surface can nest nicely at the wave vector of the commensurate 2×2 CDW order observed. Here, the elastic energy cost of lattice modulation is compensated by the total electronic energy gain via opening a gap at E_F [Fig. 3(f)] and pushing the nearby states to lower energies. Upon additional electron doping, the electron pockets become larger, deteriorating the Fermi surface nesting for the CDW phase. As the CDW phase is almost killed due to the poor Fermi surface nesting, the superconductivity occurs probably associated with the intrapocket scattering at M . They seem to fit neatly to the electronic phase diagram in Fig. 5(a).

Finally, we note that as the applied bias is lowered far below E_F , i.e., roughly at the midgap energy of -0.7 eV (Fig. 2), VIGSs with the valence band character develop equivalently near Γ , prompting substantial scattering between the Γ - and M -near VIGSs [Fig. 5(c)] at the given energy. Provided that the VBM and thus the valence-band-derived DOS are not strictly located at Γ [28,34], the scattering wave vector q_{CDW} should be smaller than that of 2×2 order. This will induce a commensurate-to-incommensurate transition of the CDW order, as observed above. The incommensurate CDW is found to run along the Γ - M direction (Fig. 2). This indicates that the VBM orients along the Γ - M direction as well [28], rather than the ΓK direction.

Our detailed STM study has revealed a commensurate 2×2 CDW phase in ultrathin SnSe₂ epitaxial films prepared on both $\sqrt{3}$ -Sn/Si and SrTiO₃ substrates. Such a collectively ordered state is found to correlate intimately with the band bending and emergent VIGSs at the semiconductor heterointerfaces. We propose an alternative mechanism associated with Fermi surface nesting between the symmetry-inequivalent electron pockets at M to account for the formation of CDW nicely. The present method of interface engineering opens up possibilities in searching for novel states of matter at the 2D limit.

This work is financially supported by the Ministry of Science and Technology of China (Grants No. 2016YFA0301004, No. 2017YFA0304600, and No. 2018YFA0305603), the National Natural Science Foundation of China (Grants No. 11774192 and No. 11634007) and in part by the Beijing Advanced Innovation Center for Future Chip.

- [1] P. Monceau, *Adv. Phys.* **61**, 325 (2012).
- [2] B. Keimer, S. Kivelson, M. Norman, S. Uchida, and J. Zaanen, *Nature (London)* **518**, 179 (2015).
- [3] H. Isobe, N. F. Q. Yuan, and L. Fu, *Phys. Rev. X* **8**, 041041 (2018).

- [4] M. Calandra, I. I. Mazin, and F. Mauri, *Phys. Rev. B* **80**, 241108(R) (2009).
- [5] A. Soumyanarayanan, M. M. Yee, Y. He, J. Van Wezel, D. J. Rahn, K. Rossnagel, E. W. Hudson, M. R. Norman, and J. E. Hoffman, *Proc. Natl. Acad. Sci. USA* **110**, 1623 (2013).

- [6] D. J. Lin, S. C. Li, J. S. Wen, H. Berger, L. Forró, H. B. Zhou, S. Jia, T. Taniguchi, K. Watanabe, X. X. Xi, and M. S. Bahramy, *Nat. Commun.* **11**, 2406 (2020).
- [7] A. Frano, S. Blanco-Canosa, E. Schierle, Y. Lu, M. Wu, M. Bluschke, M. Minola, G. Christiani, H. U. Habermeier, G. Logvenov, Y. Wang, P. A. van Aken, E. Benckiser, E. Weschke, M. L. Tacon, and B. Keimer, *Nat. Mater.* **15**, 831 (2016).
- [8] J. P. Peng, J. Q. Guan, H. M. Zhang, C. L. Song, L. Wang, K. He, Q. K. Xue, and X. C. Ma, *Phys. Rev. B* **91**, 121113(R) (2015).
- [9] X. X. Xi, L. Zhao, Z. F. Wang, H. Berger, L. Forró, J. Shan, and K. F. Mak, *Nat. Nanotechnol.* **10**, 765 (2015).
- [10] P. Chen, W. W. Pai, Y. H. Chan, A. Takayama, C. Z. Xu, A. Karn, S. Hasegawa, M. Y. Chou, S. K. Mo, A. V. Fedorov, and T. C. Chiang, *Nat. Commun.* **8**, 1 (2017).
- [11] G. Duvjir, B. K. Choi, I. Jang, S. Ulstrup, S. Kang, T. Thi Ly, S. Kim, Y. H. Choi, C. Jozwiak, A. Bostwick, E. Rotenberg, J. G. Park, R. Sankar, K. S. Kim, J. Kim, and Y. J. Chang, *Nano Lett.* **18**, 5432 (2018).
- [12] H. M. Lefcochilos-Fogelquist, O. R. Albertini, and A. Y. Liu, *Phys. Rev. B* **99**, 174113 (2019).
- [13] T. Jia, S. N. Rebec, S. Tang, K. Xu, H. M. Sohail, M. Hashimoto, D. Lu, R. G. Moore, and Z. X. Shen, *2D Mater.* **6**, 011008 (2018).
- [14] T. M. Rice and G. K. Scott, *Phys. Rev. Lett.* **35**, 120 (1975).
- [15] J. A. Wilson, *Solid State Commun.* **22**, 551 (1977).
- [16] A. Kogar, M. S. Rak, S. Vig, A. A. Husain, F. Flicker, Y. I. Joe, L. Venema, G. J. MacDougall, T. C. Chiang, E. Fradkin, J. van Wezel, and P. Abbamonte, *Science* **358**, 1314 (2017).
- [17] M. H. Whangbo and E. Canadell, *J. Am. Chem. Soc.* **114**, 9587 (1992).
- [18] T. E. Kidd, T. Miller, M. Y. Chou, and T. C. Chiang, *Phys. Rev. Lett.* **88**, 226402 (2002).
- [19] C. Guo, Z. Tian, Y. Xiao, Q. Mi, and J. Xue, *Appl. Phys. Lett.* **109**, 203104 (2016).
- [20] X. Zhou, L. Gan, W. Tian, Q. Zhang, S. Jin, H. Li, Y. Bando, D. Golberg, and T. Zhai, *Adv. Mater.* **27**, 8035 (2015).
- [21] Y. Huang, K. Xu, Z. Wang, T. A. Shifa, Q. Wang, F. Wang, C. Jiang, and J. He, *Nanoscale* **7**, 17375 (2015).
- [22] Y. B. Luo, Y. Zheng, Z. Z. Luo, S. Q. Hao, C. F. Du, Q. H. Liang, Z. Li, K. A. Khor, K. Hippalgaonkar, J. W. Xu, Q. Y. Yan, C. Wolverton, and M. G. Kanatzidis, *Adv. Energy Mater.* **8**, 1702167 (2018).
- [23] H. Wu, S. Li, M. Susner, S. Kwon, M. Kim, T. Haugan, and B. Lv, *2D Mater.* **6**, 045048 (2019).
- [24] Y. P. Song, X. W. Liang, J. G. Guo, J. Deng, G. Y. Gao, and X. L. Chen, *Phys. Rev. Mater.* **3**, 054804 (2019).
- [25] Y. M. Zhang, J. Q. Fan, W. L. Wang, D. Zhang, L. Wang, W. Li, K. He, C. L. Song, X. C. Ma, and Q. K. Xue, *Phys. Rev. B* **98**, 220508(R) (2018).
- [26] Z. B. Shao, Z. G. Fu, S. J. Li, Y. Cao, Q. Bian, H. Sun, Z. Y. Zhang, H. Gedeon, X. Zhang, L. L. J. Liu, Z. W. Cheng, F. W. Zheng, P. Zhang, and M. H. Pan, *Nano Lett.* **19**, 5304 (2019).
- [27] J. W. Zeng, E. F. Liu, Y. J. Fu, Z. Y. Chen, C. Pan, C. Y. Wang, M. Wang, Y. J. Wang, K. Xu, S. H. Cai, X. X. Yan, Y. Wang, X. W. Liu, P. Wang, S. J. Liang, Y. Cui, H. Y. Hwang, H. T. Yuan, and F. Miao, *Nano Lett.* **18**, 1410 (2018).
- [28] J. M. Gonzalez and I. I. Oleynik, *Phys. Rev. B* **94**, 125443 (2016).
- [29] J. J. Ying, H. Paudyal, C. Heil, X.-J. Chen, V. V. Struzhkin, and E. R. Margine, *Phys. Rev. Lett.* **121**, 027003 (2018).
- [30] C. L. Song, Y. L. Wang, Y. P. Jiang, Z. Li, L. Wang, K. He, X. Chen, X. C. Ma, and Q. K. Xue, *Phys. Rev. B* **84**, 020503(R) (2011).
- [31] See Supplemental Material at <http://link.aps.org/supplemental/10.1103/PhysRevB.102.241408> for details regarding substrates, FFT images, and CDW wave vectors.
- [32] S. Modesti, L. Petaccia, G. Ceballos, I. Vobornik, G. Panaccione, G. Rossi, L. Ottaviano, R. Larciprete, S. Lizzit, and A. Goldoni, *Phys. Rev. Lett.* **98**, 126401 (2007).
- [33] X. F. Wu, F. F. Ming, T. S. Smith, G. Liu, F. Ye, K. Wang, S. Johnston, and H. H. Weitering, *Phys. Rev. Lett.* **125**, 117001 (2020).
- [34] E. B. Lochocki, S. Vishwanath, X. Y. Liu, M. Dobrowolska, J. Furdyna, H. G. Xing, and K. M. Shen, *Appl. Phys. Lett.* **114**, 091602 (2019).
- [35] Q. Zhang, M. Li, E. B. Lochocki, S. Vishwanath, X. Liu, R. Yan, H.-H. Lien, M. Dobrowolska, J. Furdyna, K. M. Shen, G. J. Cheng, A. R. Hight Walker, D. J. Gundlach, H. G. Xing, and N. V. Nghyem, *Appl. Phys. Lett.* **112**, 042108 (2018).
- [36] H. Lüth, *Solid Surfaces, Interfaces and Thin Films* (Springer, Berlin, 2001), Vol. 4.
- [37] W. Monch, *Rep. Prog. Phys.* **53**, 221 (1990).
- [38] A. Kerelsky, A. Nipane, D. Edelberg, D. Wang, X. Zhou, A. Motmaendadgar, H. Gao, S. Xie, K. Kang, J. Park, J. Teherani, and A. Pasupathy, *Nano Lett.* **17**, 5962 (2017).
- [39] K. Rossnagel, L. Kipp, and M. Skibowski, *Phys. Rev. B* **65**, 235101 (2002).
- [40] K. Rossnagel, *New J. Phys.* **12**, 125018 (2010).
- [41] H. P. Hughes, *J. Phys. C: Solid State Phys.* **10**, L319 (1977).